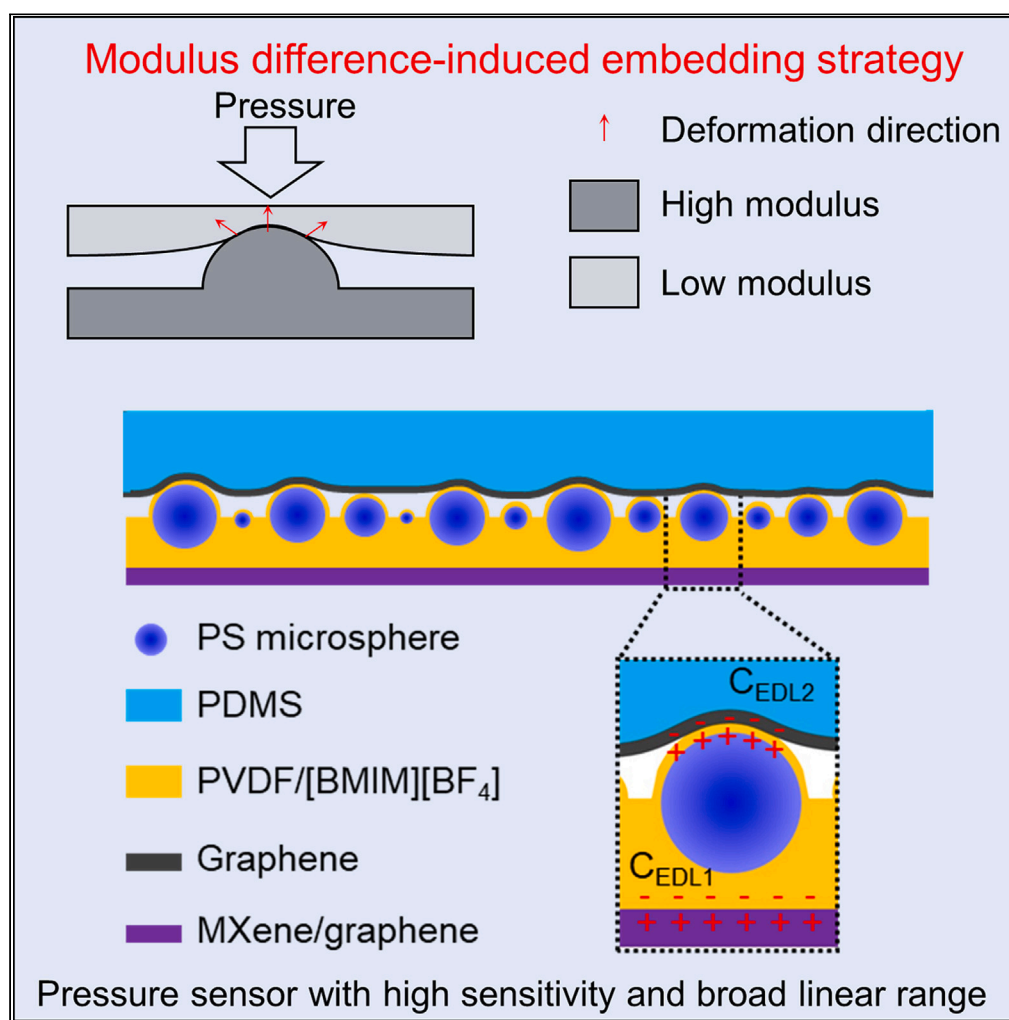**Article**

Modulus difference-induced embedding strategy to construct iontronic pressure sensor with high sensitivity and wide linear response range

Modulus difference-induced embedding strategy

Pressure-induced deformation with high modulus and low modulus regions, PS microsphere, PDMS, PVDF/[BMIM][BF$_4$], Graphene, MXene/graphene, C_{EDL1}, C_{EDL2}

Pressure sensor with high sensitivity and broad linear range

Shengjie Liu,
Zhongqian Song,
Minqi Chen, ..., Yu
Bao, Azhar
Mahmood, Li Niu

szq0819@163.com (Z.S.)
baoyu@gzhu.edu.cn (Y.B.)
lniu@gzhu.edu.cn (L.N.)

Highlights

An elastic modulus
difference-induced
embedding deformation
strategy is proposed

Microscopic observation
and simulation results
validate the strategy

The sensor exhibiting high
sensitivity, wide detection
range, and high linearity

Successful monitoring of
high-fidelity pulse
waveforms and human
motion

iScience

Article

Modulus difference-induced embedding strategy to construct iontronic pressure sensor with high sensitivity and wide linear response range

Shengjie Liu,[1,2] Zhongqian Song,[1,2,3,*] Minqi Chen,[1,2] Weiyan Li,[1,2] Yingming Ma,[1,2] Zhenbang Liu,[2] Yu Bao,[2,*] Azhar Mahmood,[1] and Li Niu[1,2,*]

SUMMARY

Sensitivity and linearity are two crucial indices to assess the sensing capability of pressure sensors; unfortunately, the two mutually exclusive parameters usually result in limited applications. Although a series of microengineering strategies including micropatterned, multilayered, and porous approach have been provided in detail, the conflict between the two parameters still continues. Here, we present an efficient strategy to resolve this contradiction via modulus difference-induced embedding deformation. Both the microscopic observation and finite element simulation results confirm the embedding deformation behavior ascribed to the elastic modulus difference between soft electrode and rigid microstructures. The iontronic pressure sensor with high sensitivity (35 kPa^{-1}) and wide linear response range (0–250 kPa) is further fabricated and demonstrates the potential applications in monitoring of high-fidelity pulse waveforms and human motion. This work provides an alternative strategy to guide targeted design of all-around and comprehensive pressure sensor.

INTRODUCTION

Increasing demand for personalized wearable healthcare monitoring systems requires high-performance sensing units to collect the reliable physiological data from human body.[1–5] Wearable pressure sensors able to convert pressure-related physiological data to machine-processable electrical signals are of great importance to sophisticated applications in intelligent healthcare and sports.[6–8] It is commonly acknowledged that the key parameters of sensitivity and linearity usually suffer from serious mutual exclusion, causing erroneous data acquisition and additional complex signal processing for further adoption.[9] In order to meet the growing demand for pressure sensor with both high sensitivity and wide linear range, the microengineering of pressure-sensitive active layer via micropatterned, porous, and multilayered packed approaches has been thoroughly investigated recently.[10–14] For example, a multiscale hierarchical interlocked design was developed to fabricate the resistive pressure sensor with high sensitivity and wide linear responsivity.[11] Meanwhile, a bioinspired magnetic composite was fabricated for the simultaneous optimization on linearity and sensitivity of capacitive pressure sensor.[15] However, the conflict between sensitivity and linearity still remains due to inevitable deformation saturation of conventional microstructures.

Continuous deformation-induced contact area variation between engineered microstructures endows the pressure sensor with ideal sensitivity and linearity. Deformation degree of the microstructures in the full range of pressure is determined by the elastic modulus of the adopted soft materials. Generally, low modulus of the microstructures contributes to effective deformation at low-pressure region, giving rising to high sensitivity, and vice versa.[16] But the previously mentioned deformation saturation usually results in poor linearity in the whole working range. Inspired by the gradient structure of human skins, multilayered modulus-gradient porous structures have been proved to be an effective approach to tackle this problem.[13,17,18] However, increased thickness of the sensors might lead to sluggish response and reduced integrability due to the multilayered configuration.[19] Therefore, developing new elastic modulus modulation strategy to optimize the deformation process of the pressure-sensitive active layer may provide a new route to construct flexible pressure sensor with balanced sensitivity and linearity.
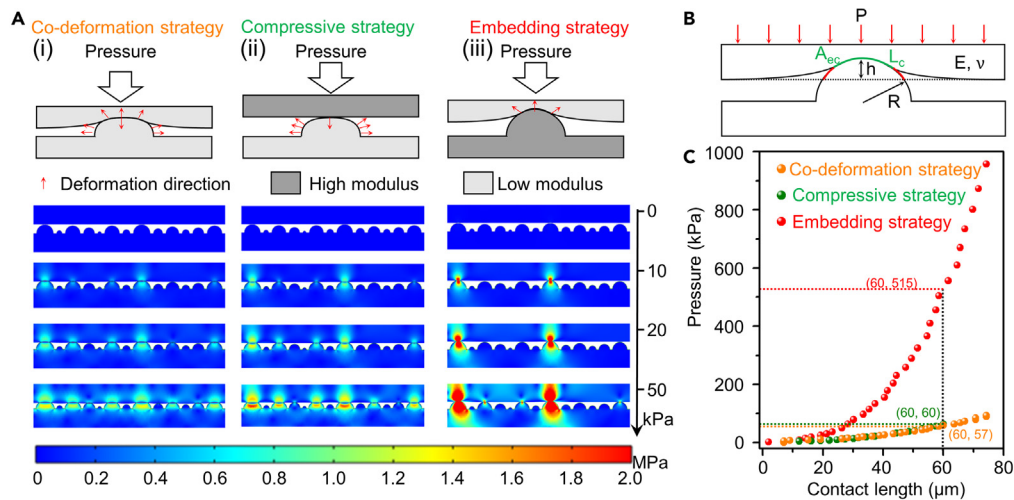
Figure 1. Design principle of the proposed modulus difference-induced embedding strategy
(A) Structural schematic and finite element simulation results of traditional co-deformation, compressive, and our proposed embedding deformation strategy.
(B) Schematic diagram and corresponding parameters under embedding deformation.
(C) Contact length-pressure curves for the conventional co-deformation, compressive, and our proposed embedding deformation strategy.

In this article, we propose an elastic modulus difference-induced embedding deformation strategy to relieve the contradiction between sensitivity and linearity of pressure sensor. High-modulus polystyrene microspheres embedded into polyvinylidene fluoride (PVDF) film and low-modulus polydimethylsiloxane (PDMS) conductive film are served as microstructured and counter electrodes, respectively. Unlike the compressive deformation process of conventional soft microstructures, the undeformable high-modulus polystyrene microspheres tend to embed into soft PDMS conductive film under external pressure, contributing to embedding deformation of PDMS conductive film. The finite element simulation results demonstrate that such embedding deformation still occurs in high external pressure region, giving rising to continuous variation in contact area between polystyrene microspheres and PDMS. The as-fabricated pressure sensor exhibits high sensitivity, wide detection range, and high linearity. Meanwhile, the characteristic of response hysteresis and stability degradation can be improved owing to the special embedding deformation process. To highlight the advantages of the pressure sensors in different applications, we demonstrate the use of the pressure sensor for pulse waveform and sport monitoring. This work provides a universal strategy for constructing pressure sensors with both high sensitivity and linearity.

RESULTS AND DISCUSSION

Design principle of the proposed modulus difference-induced embedding strategy

Although the sensitivity and linearity can be well modulated via various microengineering design and fabrication methods, linearity at pressure higher than 100 kPa is fundamentally limited by the deformation saturation of the soft microstructures.[20] In order to slow down the deformation saturation process, we innovatively propose an embedding deformation strategy using undeformable high-modulus microstructures and low-modulus even-surfaced counter electrode. To elucidate the underlying mechanism to achieve both high sensitivity and linearity over a broad pressure regime, three representative models including conventional co-deformation, compressive, and our proposed embedding deformation strategy are developed and corresponding deformation and stress distribution are investigated via finite element analysis (Figure 1). Traditional design based on low-modulus microstructures and counter electrode usually leads to co-deformation of them as shown in Figure 1A(i). Meanwhile, although high-modulus counter electrode is adopted, low-modulus microstructures can be easily compressed under external pressure and then quickly reach deformation saturation state (Figure 1A(ii)). Distinct from conventional co-deformation and compressive strategy, the undeformable high-modulus microstructures and low-modulus even-surfaced electrode are adopted. Such modulus difference will lead to embedding deformation of high-modulus microstructures into low-modulus even-surfaced electrode. As shown in Figure 1A(iii), the proposed

embedding deformation strategy demonstrates fewer stress concentration points and endows the structures with enhanced capacity to bear higher stress, leading to more variable deformation spaces at high-pressure regime. High-modulus hemispherical structures are embedded into flat elastics under external pressure, resulting in locally embedding deformation. Such modulus difference-induced embedding deformation strategy could significantly slow down the deformation saturation process and guarantee continuous changes in contact area between the microstructures and counter electrode, giving rising to constant linearity even at high-pressure regime.

In order to figure out the underlying principle of the modulus difference-induced embedding deformation behavior, a simplified model is constructed as shown in Figure 1B. It is assumed that the even-surfaced counter electrode is fully elastic and no irreversible deformation occurs. Meanwhile, the high-modulus microstructure is undeformable. The embedded depth (h) of the micro-hemisphere can be expressed as

$$h = \left[\frac{3(1 - \nu^2)}{4E}\right]^{2/3}\left(\frac{P^2}{R}\right)^{1/3}$$

where E and ν are the elastic modulus and Poisson ratio of the flat counter electrode, respectively, and R is radius of the micro-hemisphere and P is the applied pressure. The embedded depth, contact length (L_c), and contact area (A_c) are highly dependent on the elastic modulus and radius of the micro-hemisphere. Low-modulus and high-modulus micro-hemispheres are adopted for the conventional co-deformation model and our embedding deformation strategy, respectively. As shown in Figure 1A, low-modulus microstructures result in larger deformation at the same pressure, contributing to larger contact length than conventional co-deformation model. It means that higher elastic modulus of even-surfaced counter electrode and larger radius of micro-hemisphere endow the pressure sensor with capacity to bear higher pressure. Coupled with height gradient among the random distributed micro-hemispheres, smaller micro-hemispheres will be then embedded into the electrode after the bigger ones embedded in, leading to gradually variation in contact area between the two electrodes over a wide pressure regime. As shown in Figure 1C, the embedding deformation strategy exhibits substantial growth with increasing contact length in comparison to the conventional co-deformation and compressive strategies, subsequently contributing to enhanced sensitivity in high-pressure regime.

Fabrication, structure, and working mechanism of the iontronic pressure sensor

In our work, we construct an iontronic pressure sensor by integrating two Janus films, i.e., top PDMS/graphene conductive electrode and bottom microstructured electrode, as shown in Figures 2A and S1. Detailed fabrication processes of the two Janus films are demonstrated in Figures S2 and S3. The top PDMS/graphene conductive electrode is prepared via spray coating and subsequent blade coating method, endowing the electrode with even and smooth conductive surface (Figure 2B). The bottom microstructured electrode is fabricated by transfer printing and subsequent blade coating procedure (Figure S3). The patterned conductive electrodes are firstly prepared via vacuum filtration of MXene ($Ti_3C_2T_x$)/graphene suspension and then transferred onto glass substrate by transfer printing method (Figures S4–S6). After subsequently blade coating of PVDF/1-butyl-3-methylimidazolium tetrafluoroborate ([BMIM][BF$_4$]) solution containing polystyrene (PS) microspheres (Figure S7), microstructured electrodes can be obtained after the removal of solvents. As shown in Figure 2C, PS microspheres are randomly wrapped into PVDF polymer matrix, and the MXene/graphene conductive electrode is tightly combined with polymer matrix. The cross-sectional elemental mapping images of the microstructured electrode exhibit that the boron and nitrogen elements are uniformly distributed across the whole microstructured electrode, indicating the uniform distribution of [BMIM][BF$_4$] ionic liquid. Meanwhile, the local distribution of fluorine and titanium elements confirms the Janus feature of the microstructured electrode, where MXene/graphene electrode and micro-hemispheres serve as the conductive electrode to collect the charges and pressure-sensitive active units, respectively.

In order to confirm the modulus-induced embedding deformation process, *in situ* optical microscopic images and *ex situ* cross-sectional morphologies of the iontronic pressure sensor under different pressure are investigated. As shown in Figure 2D, the microstructured electrode exhibits almost the same morphologies under 0 and 312 kPa and no significant changes in diameter of PS microspheres are observed, indicating their undeformable characteristics due to their high elastic modulus. Meanwhile, the *ex situ* SEM results in Figure 2E confirm the embedding deformation of high-modulus microstructures into low-modulus
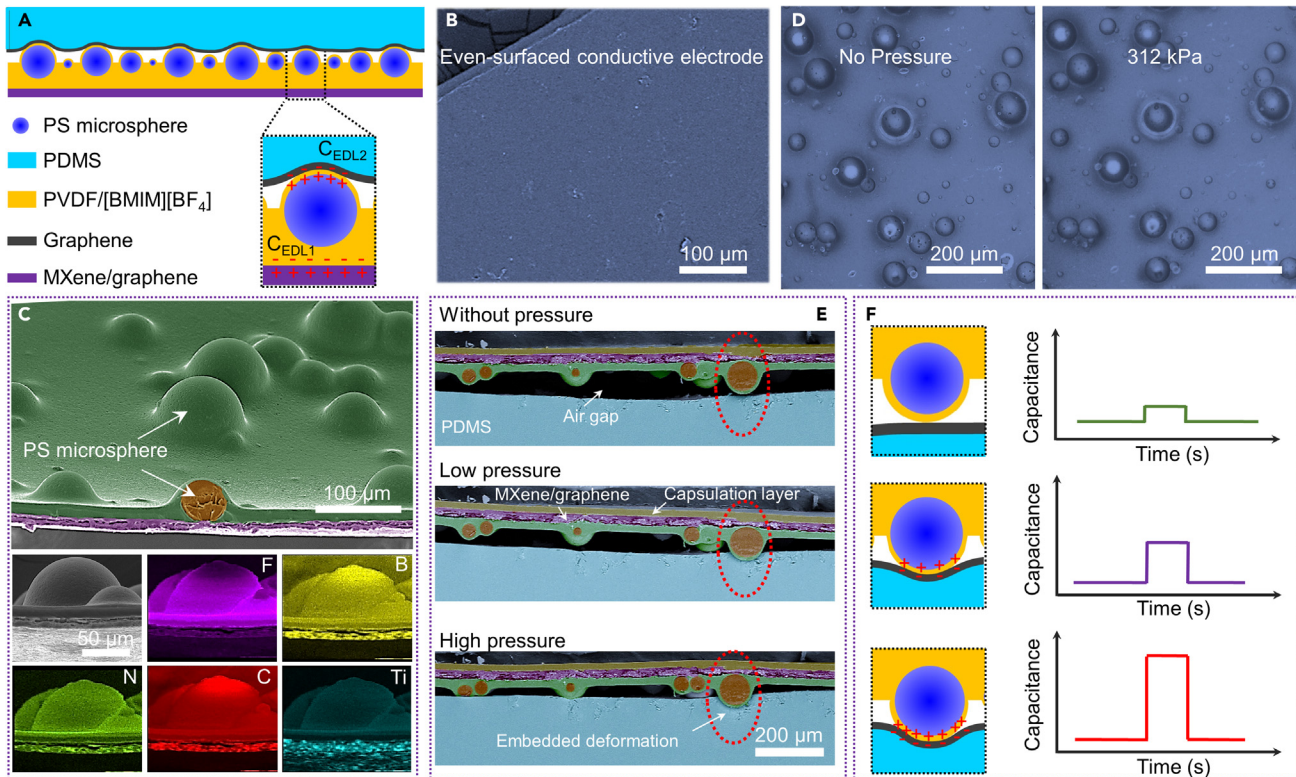
Figure 2. Fabrication, structure, and working mechanism of the iontronic pressure sensor

(A) Schematic illustration and exploded view of the iontronic pressure sensor.

(B) Surface morphology of even-surfaced conductive electrode.

(C) Cross-sectional morphology and corresponding element mapping images of microstructured electrode.

(D) Optical microscopic images of microstructured electrode at pressure of 0 and 312 kPa.

(E) *Ex situ* cross-sectional morphologies of the iontronic pressure sensor under different pressure.

(F) Schematic for the sensing mechanism of the iontronic pressure sensor.

PDMS elastomer. Since the separation of top microstructured electrode with the bottom electrode, the pure electrical double-layer (EDL) capacitance is dominated without external pressure (Figures 2E and 2F). The micro-domes with larger diameter are firstly embedded into the PDMS/graphene electrode under low external pressure, leading to the aggregation of EDL charges at the iontronic interface between the two electrodes and enhanced EDL capacitance of the iontronic pressure sensor. With the increasing external pressure, these high-modulus micro-domes start to embed into the PDMS/graphene electrode, giving rising to large contact area at the interfaces and further increasing the EDL capacitance of the sensor.

Considering the special modulus difference-induced embedding deformation process, it is reasonable to assume that the sensitivity and linear sensing range of the iontronic pressure sensor can be readily modulated by changing the elastic modulus of even-surfaced electrode. The simplified equivalent circuit diagram of the iontronic pressure sensor in Figures 1A and S8 demonstrates two EDL capacitors formed at the MXene/graphene interfaces (C_{EDL1}) and graphene interfaces (C_{EDL2}), which are connected in series with a bulk resistance and in parallel with the capacitance induced by the two electrodes (C_E). The capacitance of the iontronic pressure sensor is dominated by the C_{EDL2}, which is determined by the interfacial contact area A_c at the interfaces (Figure 2A). The effective contact area (A_{ec}) can be expressed as

$$A_{ec} = 2\alpha\pi\left[\frac{3RP(1-\nu^2)}{4E}\right]^{2/3}$$

where α is a correction factor that depends on embedded depth h of the micro-hemisphere due to the incomplete contact area at the interfaces (red region in Figure 1B). Therefore, for a specific radius of the
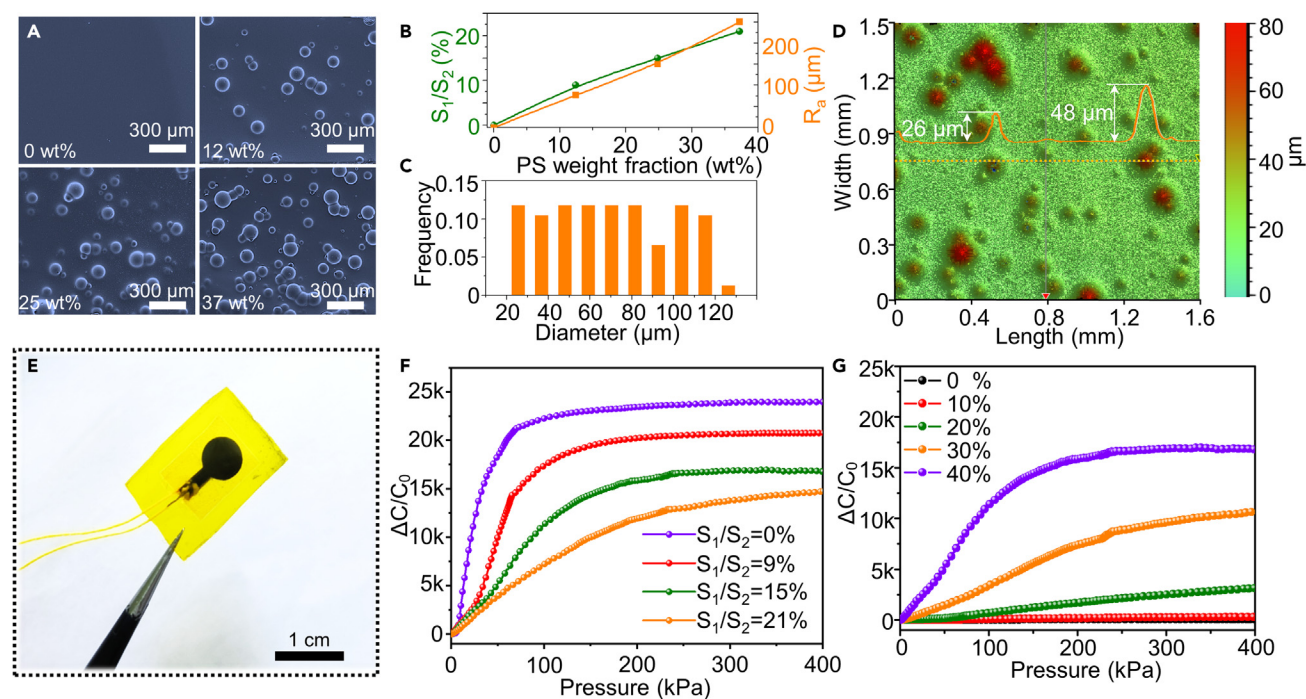
Figure 3. Sensing performance optimization of the iontronic pressure sensor

(A) Surface SEM images of the microstructured electrodes with different weigh fraction of PS microspheres.

(B) Variation of S_1/S_2 and R_a with weight fraction of PS microspheres.

(C) Size distribution of the exposed PS microspheres.

(D) Surface height mapping image of the microstructured electrodes with 12 wt % PS microspheres.

(E) Photograph of the as-fabricated iontronic pressure sensor.

(F) Pressure-response curves of iontronic pressure sensors based on microstructured electrodes with different weigh fraction of PS microsphere.

(G) Pressure-response curves of iontronic pressure sensors based on microstructured electrodes with different weight fraction of [BMIM][BF$_4$] (PS microsphere: 15 wt %).

micro-hemisphere, it can be deduced that higher elastic modulus and lower Poisson's ratio lead to smaller effective contact area under the same external pressure. It can also be supported by the simulation results based on even-surfaced electrode with different Young's moduli of 0.5, 1, and 10 MPa (Figure S9). Under the same pressure of 200 kPa, higher elastic modulus of the even-surfaced electrode contributes to smaller embedding depth and lower contact area. It means that the embedding deformation process is retarded, which will broaden the linear sensing range but compromise the sensitivity simultaneously.

Sensing performance optimization of the iontronic pressure sensor

To investigate the influence of density of micro-domes and weight fraction of [BMIM][BF$_4$] on the sensing performance of the iontronic pressure sensors, a series of iontronic pressure sensors are fabricated. The microstructured electrodes with different weigh fractions of PS microspheres (0, 12, 25, and 37 wt %) are prepared and corresponding surface morphologies are demonstrated in Figure 3A. More raised micro-domes can be observed with increasing weight fraction of PS microspheres. The area proportions of exposed PS microspheres defined as S_1/S_2 are calculated to be 9%, 15%, and 21% with the increasing weight fraction of PS microspheres (Figure S10), resulting in linear increase in surface roughness (R_a) (Figure 3B). Meanwhile, the size distribution of the exposed PS microspheres almost homogeneously ranges from 25 to 115 μm (Figure 3C). Coupled with the increasing R_a, the random distribution and discrete diameter of the micro-domes might enable enhanced sensing linearity and sensing range.[21] Compared with the SEM results, the surface height mapping image of the microstructured electrode demonstrates similar morphology, and the height values of 26 and 48 μm confirm the hemispherical microstructures (Figure 3D).

The iontronic pressure sensors with a thickness of 0.5 mm are fabricated by integrating the top even-surfaced conductive electrode with the microstructured electrode and encapsulated with flexible polyimide
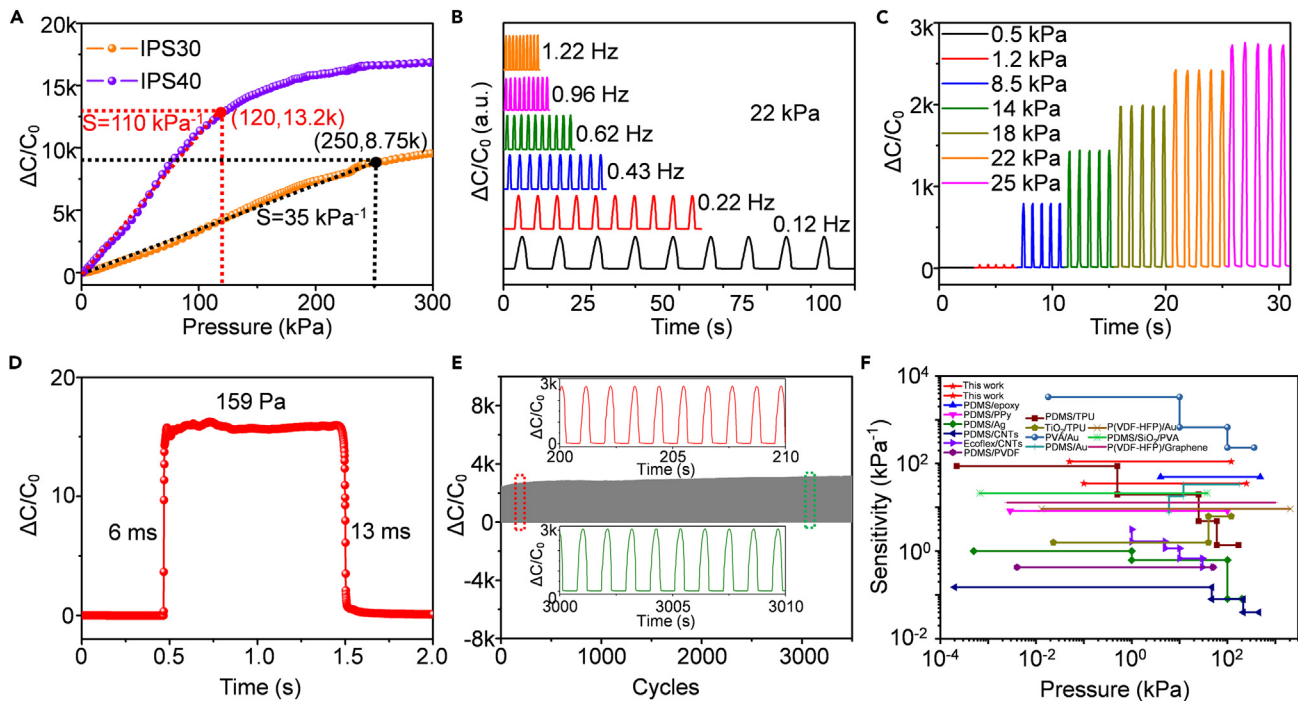
Figure 4. Detailed sensing properties of the iontronic pressure sensor

(A) Pressure-response curves of the iontronic pressure sensors based on microstructured electrode with different weight fractions (30, 40 wt %) of ionic liquid ($S_1/S_2 = 15\%$).

(B) Dynamic response to 22 kPa at frequencies from 0.12 to 1.22 Hz.

(C) Repeatability of the iontronic pressure sensor at different external pressures (0.93 Hz).

(D) Response and recovery time of the iontronic pressure sensor at 159 Pa.

(E) Cycling stability of the sensor under repetitive pressure loading of 30 kPa.

(F) Comparison of the sensitivity and linear sensing range of the iontronic pressure sensor with previous reports.

film, as shown in Figure 3E. Pressure responses of the iontronic pressure sensors based on microstructured electrode with different S_1/S_2 ratio are investigated as demonstrated in Figure 3F, where C_0 and ΔC represent the initial capacitance and the real-time capacitance changes under external pressure, respectively. It can be observed that the S_1/S_2 ratio significantly affects the sensing behaviors of the iontronic pressure sensors. The pressure sensor without PS microspheres shows rapid increase and saturation in capacitance due the absence of deformable microstructures. Although lower S_1/S_2 ratio contributes to higher sensitivity, the linearity and sensing range of the iontronic pressure sensors are significantly improved with increasing S_1/S_2 ratio of the microstructured electrode. The sensing range of the iontronic pressure sensor can reach up to ~300 kPa with increasing S_1/S_2 ratio. Meanwhile, the linear range of the sensor can be broadened up to ~200 kPa. In addition, the performance of our fabricated iontronic pressure sensor is highly reproducible and the sensors fabricated from different batches exhibit similar sensing behaviors (Figure S12). Meanwhile, the sensing behaviors of the iontronic pressure sensors based on the microstructured electrode with different weight fraction of ionic liquid are further investigated. As shown in Figure 3G, the iontronic pressure sensors based on microstructured electrode with higher ionic liquid content give rise to higher maximum capacitance. Even though higher ionic liquid content contributes to higher sensitivity of the pressure sensor, the linear sensing range might be compromised. We speculate that the excessive ionic liquid within the microstructured electrode could be squeezed out upon high-pressure compression and further contribute to charge saturation at the interfaces. Hence, the sensing performances of the iontronic pressure sensor can be well modulated via changing the concentration of ionic liquid and S_1/S_2 ratio.

Detailed sensing properties of the iontronic pressure sensor

Given their superior sensitivity, linearity, and sensing range, the iontronic pressure sensors based on microstructured electrode ($S_1/S_2 = 15\%$) with different weight fractions (30, 40 wt %) are chosen to investigate their detailed sensing performances. Corresponding pressure-response curves are demonstrated in Figure 4A.

The iontronic pressure sensor (ionic liquid: 30 wt %) shows an ultrabroad and linear sensing range up to 250 kPa, while it still maintains high sensitivity of 35 kPa^{-1}. The sensitivity can be further improved to 110 kPa^{-1} by increasing the content of ionic liquid from 30 to 40 wt %. Meanwhile, the sensor still exhibits a linear sensing range from 0 to 120 kPa. The dynamic response behavior of the sensor is also investigated as shown in Figure 4B. The sensor exhibits similar and reversible $\Delta C/C_0$ amplitude at 22 kPa from 0.12 to 1.22 Hz, demonstrating its capacity for frequency analysis of dynamic pressure. In addition, the real-time response to periodic pressure (0.5, 1.2, 8.5, 14, 18, 22, and 25 kPa) indicates excellent reproducibility of the sensor (Figure 4C).

Meanwhile, thanks to the special embedding deformation process of the microstructures, the sensor exhibits ultrafast response (6 ms) and recovery time (13 ms), allowing real-time dynamic and high-fidelity pressure acquisition (Figure 4D). The minimum pressure detection limit of the sensor is measured to be ~14 Pa (Figure S13). The pressure sensor also exhibits almost overlapped loading and unloading curves, indicating slight hysteresis and good recovery capabilities (Figure S14). The cycling stability of the iontronic pressure sensor is evaluated under repetitive pressure loading of 30 kPa (Figure 4E). The iontronic pressure sensor demonstrates slight shift and subsequent stabilization during the 3500 repetitive loading/unloading test. The slight shift to high capacitance at the initial ~300 cycles might be ascribed to the presence of some unstable interfaces at the even-surfaced conductive graphene electrode. The iontronic pressure sensor exhibits nearly overlapping pressure-response curves before and after the cycling test, indicating good cyclic stability (Figure S15). Meanwhile, the initial and final several cycles in inset of Figure 4E show similar on/off response amplitude, indicating its good sensing reversibility and reproducibility. It is assumed that such reproducibility and stability are ascribed to the embedding deformation process, where the local impression of the even-surfaced PDMS film could rapidly recover to its initial state. Compared with previously reported sensors, our iontronic pressure sensor exhibits comparable or even higher sensitivity and broader linear sensing range than PDMS-based pressure sensors,[22–27] and other polymer-based pressure sensors[28–34] (Figure 4F). It is worth noting that most of the reported pressure sensors exhibit multistep sensitivity across the whole sensing range, indicating nonlinear sensing behavior within the sensing range. However, our pressure sensor exhibits constant sensitivity within the sensing range up to 250 kPa, indicating broad linear sensing range. It is reasonable to assume that the linear sensing range and sensitivity of the pressure sensors can be further optimized via the proposed embedding deformation strategy.

Applications in monitoring of high-fidelity pulse waveforms and human motion

Pulse waveforms can directly reflect the health status of human body.[35] Considering the high sensitivity, linearity, and rapid response properties, the iontronic pressure sensor could satisfy the demand for high-fidelity monitoring of epidermal pulse waveforms. Continuous contraction and diastole of the heart leads to the formation of pulse waveforms. As shown in Figure 5A, a cyclic pulse waveform mainly contains several feature points, such as starting point, percussion wave (P), tidal wave (T), incisura wave, and dicrotic wave (D). Some critical cardiovascular information such as arterial elasticity and blood vessel aging can be obtained via the transformation and feature point extraction of pulse waveforms. Here, a 25-year-old asymptomatic male volunteer after strenuous exercise was recruited for real-time pulse waveforms acquisition and analysis during the 15 min rest period. The pulse waveforms recorded at 0, 1, 3, 6, 9, and 15 min are demonstrated in Figure 5B, indicating stable periodic cycles with low-level noise ratio. The pulse rate can be obtained from corresponding frequency spectra (Figure S16). The enlarged views at different times indicate a typical slippery pulse, which is consistent with previously reported results.[36,37] Such a slippery pulse conforms to the real pulse symptom consistent with the physiological stage in young adulthood due to their good vascular elasticity and low peripheral resistance. During the continuous 15 min rest period, as shown in Figure 5C, the increasing amplitudes of P and D points are ascribed to the transformation of vessel from dilated status to contraction status.[38] The strenuous exercise leads to rapid rising in volunteers' pulse rate, reaching up to 133 beats/min. After 15 min rest, the pulse rate gradually returns to normal levels (96 beats/min) (Figure 5D). The time delay (Δt) between the P wave (p point) and T wave (t point) as well as the aging index (AI) are calculated with the help of the corresponding first and second derivative curves (Figures 4A and S17). As shown in Figures 5E and 5F, the gradual increasing Δt and AI values also confirm the transformation of vessel from dilated status to contraction status.[39] Therefore, proper exercise facilitates the expansion of vessels and further enhances the systolic/diastolic capability of vessels, improving the elasticity of blood vessels. In addition, the iontronic pressure sensors can be attached onto different location of human body such as the arms, wrists, backs of hands, neck, fingertips, and fingers to
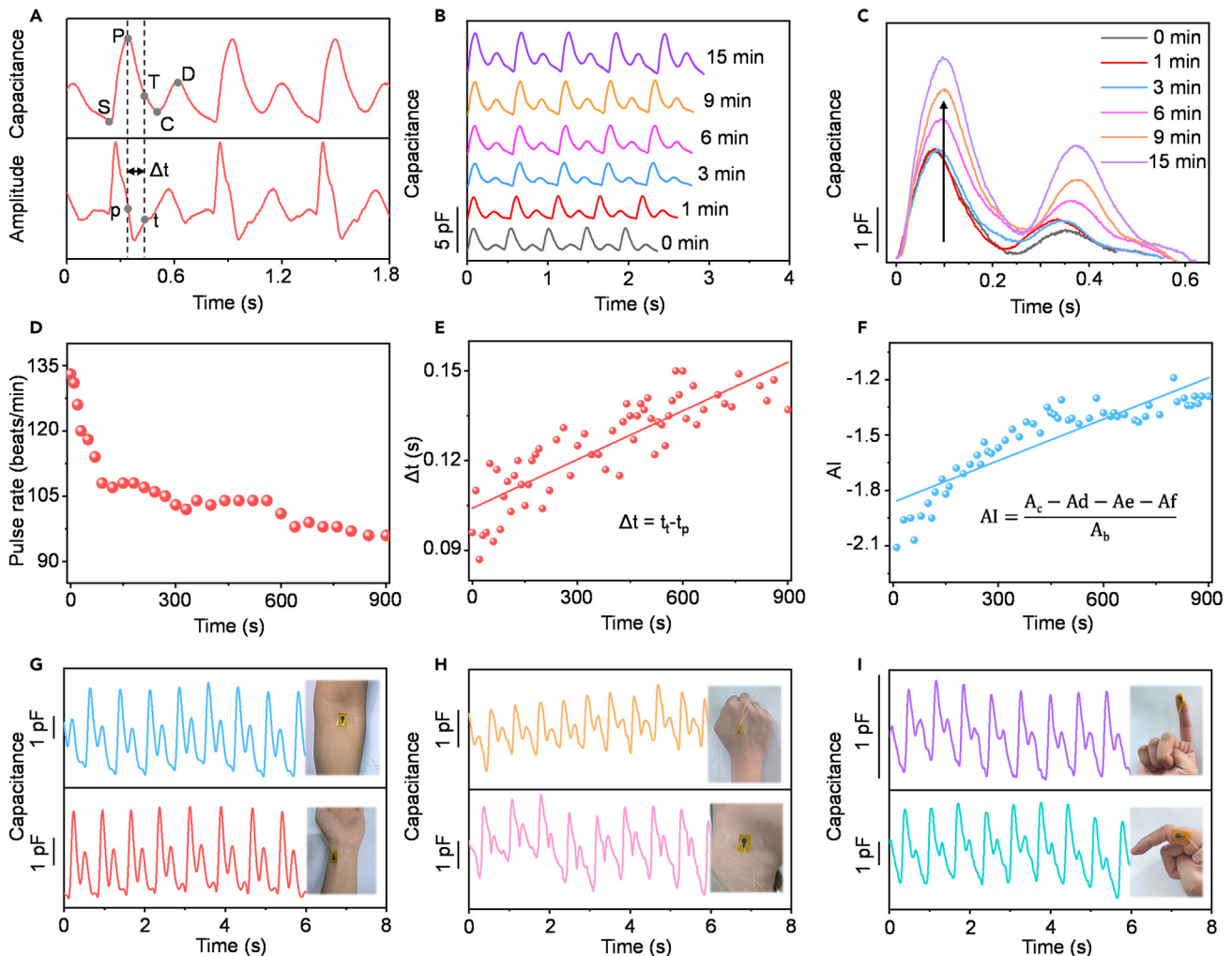
Figure 5. Versatile monitoring of high-fidelity pulse waveforms
(A) Typical pulse waveforms, first derivative signals, and corresponding feature points.
(B) Real-time monitoring of pulse waveforms at wrist for a volunteer during a 15 min rest period after vigorous activity.
(C) Pulse waveforms at different rest times.
(D–F) Variation in (D) pulse rate, (E) Δt, and (F) AI during the 15 min rest period.
(G–I) Real-time recording of pulse signals at different human body location.

capture the pulse waveforms of the volunteer (Figures 5G–5I), demonstrating potential application for comprehensive health monitoring and disease assessment.

Due to its broad linear range and high sensitivity, our fabricated iontronic pressure sensor can be used for monitoring of human body motion. In order to show the superiority of the iontronic pressure sensor, six devices are fixed on a starting block to record the pressure data during a start of a race (Figure 6A). Two three-channels capacitance recording modules are adopted to collect the capacitance data, which are transmitted to computer via USB communication (Figure 6B). Starting positions especially for sprints directly determine the final results of a competitive track race. As shown in Figure 6C, the start of a race includes four decomposition movements: preparatory action, ready action, buns lift, and thrusting the body. The iontronic pressure sensors can percept the pressure variation during four decomposition movements. The channel 2 and 5 bear higher contact pressure than the other four sensors, and the explosive time of the left and right feet are about 0.22 and 0.19 s (Figure 6D). The pressure data might allow us to inspect the abnormal actions or evaluate the training intensity for scientific training. It is anticipated that our iontronic pressure sensor will provide significant support for the development of intelligent sports in the near future.
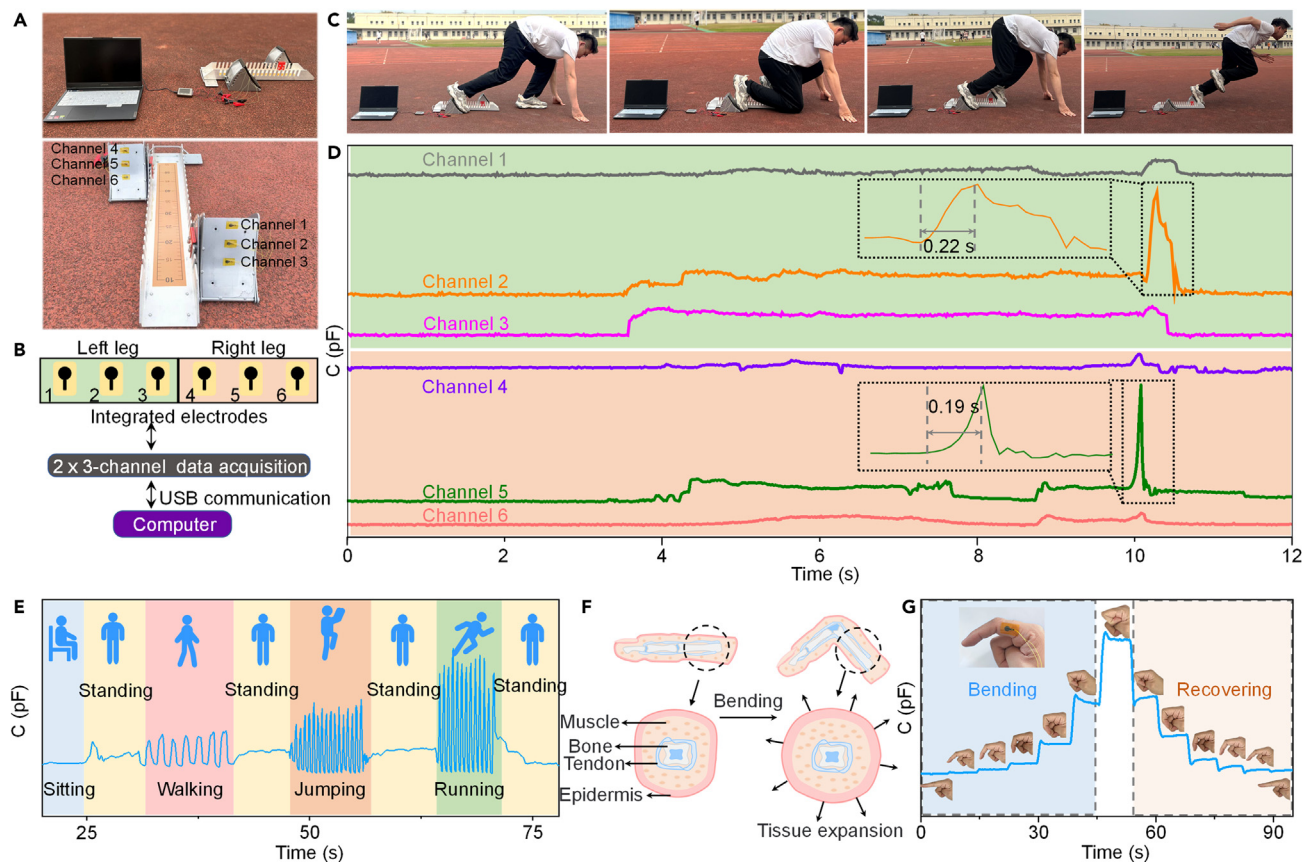
Figure 6. Versatile monitoring of human body motion
(A) Photograph of the platform for pressure monitoring during a start of a race.
(B) Flow diagram for data collection during a start of a race.
(C) Photographs showing the four decomposition movements of a start of a race.
(D) Collected data from the six iontronic pressure sensor integrated within the starting block.
(E) Real-time monitoring of the whole motion process, including sitting, standing, walking, jumping, and running.
(F) Schematic of a finger under straight and bent status and corresponding cross-sectional enlarged views.
(G) Capacitance response to different bending angles.

Considering the ultrabroad sensing range of the iontronic pressure sensor, it can be used for foot-pressure monitoring. The sensor is integrated into the insole as a gait detector to monitor the movements of the human body (Figure 6E). The sensor exhibits distinguishable features during the whole movement (sitting, standing, walking, jumping, and running). It demonstrates different output frequency and amplitude for walking, jumping, and running motions. For example, a noticeable increase in capacitance is observed due to the large impact force during running.

In addition, this iontronic pressure sensor can also be exploited as a tool to detect the bending state of finger. During the bending process, the tissue around the phalanges of the finger will be compressed and swelled (Figure 6F). When the iontronic pressure sensor is fixed onto the phalange position, finger bending will result in compression of the sensor and increasing output capacitance values. As shown in Figure 6G, the capacitance altitudes of the iontronic pressure sensor increase with the enlargement of the bending angles and decrease to initial state with the straight angles of finger. Given the curvy features and large strain of the joints, comparing with the traditional monitoring mode that attached at the joints, this strategy avoids the possible slippage between finger and sensor and will contribute to accurate monitoring of bending angles. In addition, the iontronic pressure sensor can also be used to monitor whether the postures during movements are standard (Figure S18). The iontronic pressure sensors demonstrate diversified functions in monitoring of human body motions and may provide more comprehensive and reliable information for sports monitoring and healthcare.

Conclusion

In this work, we propose a modulus difference-induced embedding deformation strategy to relieve the contradiction between sensitivity and linear sensing range of wearable pressure sensors. The low-modulus even-surfaced graphene/PDMS conductive electrode and high-modulus microstructured polymer ionic film are fabricated for directly assembly of the iontronic pressure sensor. Our designed high-modulus microstructures tend to embed into low-modulus even-surfaced elastomer under external pressure rather than the common compression deformation of microstructures for traditional design strategy. Combined with the supercapacitance at the interfaces, this special modulus difference-induced imbedding deformation behavior endows the iontronic pressure sensor with high sensitivity, ultrabroad linear range, and rapid response. Based on these advantages, the iontronic pressure sensors are used as proof of concept for monitoring of pulse waveforms and human motion. This proposed strategy provides new guidance for designing high-performance pressure sensors but also call for more exploration for fundamental mechanisms behind modulus modulation.

Limitations of the study

We did not investigate the influence of diameter, height, and distribution of high-modulus microstructures on the properties of the iontronic pressure sensors. The quantitative relationship between modulus and linear sensing range is still needed to be defined.

STAR★METHODS

Detailed methods are provided in the online version of this paper and include the following:

- KEY RESOURCES TABLE
- RESOURCE AVAILABILITY
  - ○ Lead contact
  - ○ Materials availability
  - ○ Data and code availability
- METHOD DETAILS
  - ○ Materials and instruments
  - ○ Preparation of the even-surfaced conductive electrode
  - ○ Preparation of microstructured ionic polymer film
  - ○ Fabrication and application of the iontronic pressure sensor
  - ○ Finite element analysis

SUPPLEMENTAL INFORMATION

Supplemental information can be found online at https://doi.org/10.1016/j.isci.2023.107304.

AUTHOR CONTRIBUTIONS

S.Z. and N.L. conceived and designed the experiments. L.S., C.M., B.Y., L.W., M.A., and L.Z. prepared materials, performed the experiments, and analyzed experimental data. S.Z. wrote the manuscript. B.Y. and M.Y. revised the manuscript, S.Z., L.W., B.Y., and N.L. supervised all the aspects of this work and provided financial support. All authors discussed the results and contributed to the paper.

DECLARATION OF INTERESTS

The authors declare no competing interests.

REFERENCES

1. Cai, Y., Shen, J., Yang, C.W., Wan, Y., Tang, H.L., Aljarb, A.A., Chen, C., Fu, J.H., Wei, X., Huang, K.W., et al. (2020). Mixed-dimensional MXene-hydrogel heterostructures for electronic skin sensors with ultrabroad working range. Sci. Adv. 6, eabb5367. https://doi.org/10.1126/sciadv.abb5367.

2. Zhao, C., Wang, Y., Tang, G., Ru, J., Zhu, Z., Li, B., Guo, C.F., Li, L., and Zhu, D. (2022). Ionic Flexible Sensors: Mechanisms, Materials, Structures, and Applications. Adv. Funct. Mater. 32, 2110417. https://doi.org/10.1002/adfm.202110417.

3. Chen, M., Li, P., Wang, R., Xiang, Y., Huang, Z., Yu, Q., He, M., Liu, J., Wang, J., Su, M., et al. (2022). Multifunctional Fiber-Enabled Intelligent Health Agents. Adv. Mater. 34, 2200985. https://doi.org/10.1002/adma.202200985.

4. You, I., Mackanic, D.G., Matsuhisa, N., Kang, J., Kwon, J., Beker, L., Mun, J., Suh, W., Kim, T.Y., Tok, J.B.H., et al. (2020). Artificial multimodal receptors based on ion relaxation dynamics. Science 370, 961–965. https://doi.org/10.1126/science.aba5132.

5. Kim, T., Kim, J., You, I., Oh, J., Kim, S.P., and Jeong, U. (2022). Dynamic tactility by position-encoded spike spectrum. Sci. Robot. 7, eabl5761. https://doi.org/10.1126/scirobotics.abl5761.

6. Kong, H., Song, Z., Li, W., Bao, Y., Qu, D., Ma, Y., Liu, Z., Wang, W., Wang, Z., Han, D., and Niu, L. (2021). Skin-Inspired Hair-Epidermis-Dermis Hierarchical Structures for Electronic Skin Sensors with High Sensitivity over a Wide Linear Range. ACS Nano 15, 16218–16227. https://doi.org/10.1021/acsnano.1c05199.

7. Niu, H., Li, H., Gao, S., Li, Y., Wei, X., Chen, Y., Yue, W., Zhou, W., and Shen, G. (2022). Perception-to-Cognition Tactile Sensing Based on Artificial-Intelligence-Motivated Human Full-Skin Bionic Electronic Skin. Adv. Mater. 34, e2202622. https://doi.org/10.1002/adma.202202622.

8. Miao, P., Wang, J., Zhang, C., Sun, M., Cheng, S., and Liu, H. (2019). Graphene Nanostructure-Based Tactile Sensors for Electronic Skin Applications. Nano-Micro Lett. 11, 71. https://doi.org/10.1007/s40820-019-0302-0.

9. Tang, X., Wu, C., Gan, L., Zhang, T., Zhou, T., Huang, J., Wang, H., Xie, C., and Zeng, D. (2019). Multilevel Microstructured Flexible Pressure Sensors with Ultrahigh Sensitivity and Ultrawide Pressure Range for Versatile Electronic Skins. Small 15, e1804559. https://doi.org/10.1002/smll.201804559.

10. Ruth, S.R.A., Feig, V.R., Tran, H., and Bao, Z. (2020). Microengineering Pressure Sensor Active Layers for Improved Performance. Adv. Funct. Mater. 30, 2003491. https://doi.org/10.1002/adfm.202003491.

11. Huang, L., Zeng, R., Tang, D., and Cao, X. (2022). Bioinspired and multiscale hierarchical design of a pressure sensor with high sensitivity and wide linearity range for high-throughput biodetection. Nano Energy 99, 107376. https://doi.org/10.1016/j.nanoen.2022.107376.

12. Lee, Y., Park, J., Cho, S., Shin, Y.E., Lee, H., Kim, J., Myoung, J., Cho, S., Kang, S., Baig, C., and Ko, H. (2018). Flexible Ferroelectric Sensors with Ultrahigh Pressure Sensitivity and Linear Response over Exceptionally Broad Pressure Range. ACS Nano 12, 4045–4054. https://doi.org/10.1021/acsnano.8b01805.

13. Pyo, S., Lee, J., Kim, W., Jo, E., and Kim, J. (2019). Multi-Layered, Hierarchical Fabric-Based Tactile Sensors with High Sensitivity and Linearity in Ultrawide Pressure Range. Adv. Funct. Mater. 29, 1902484. https://doi.org/10.1002/adfm.201902484.

14. Chen, J., Zhu, G., Wang, J., Chang, X., and Zhu, Y. (2023). Multifunctional Iontronic Sensor Based on Liquid Metal-Filled Ho llow Ionogel Fibers in Detecting Pressure, Temperature, and Proximity. ACS Appl. Mater. Interfaces 15, 7485–7495. https://doi.org/10.1021/acsami.2c22835.

15. Ji, B., Zhou, Q., Hu, B., Zhong, J., Zhou, J., and Zhou, B. (2021). Bio-Inspired Hybrid Dielectric for Capacitive and Triboelectric Tactile Sensors with High Sensitivity and Ultrawide Linearity Range. Adv. Mater. 33, 2100859. https://doi.org/10.1002/adma.202100859.

16. Wang, J., Cui, X., Song, Y., Chen, J., and Zhu, Y. (2023). Flexible iontronic sensors with high-precision and high-sensitivity detection for pressure and temperature. Compos. Commun. 39, 101544. https://doi.org/10.1016/j.coco.2023.101544.

17. Zhang, X., Hu, Z., Sun, Q., Liang, X., Gu, P., Huang, J., and Zu, G. (2023). Bioinspired Gradient Stretchable Aerogels for Ultrabroad-Range-Response Pressure-Sensitive Wearable Electronics and High-Efficient Separators. Angew. Chem. Int. Ed. 62, e202213952. https://doi.org/10.1002/anie.202213952.

18. Song, S., Zhang, C., Li, W., Wang, J., Rao, P., Wang, J., Li, T., and Zhang, Y. (2022). Bioinspired engineering of gradient and hierarchical architecture into pressure sensors toward high sensitivity within ultra-broad working range. Nano Energy 100, 107513. https://doi.org/10.1016/j.nanoen.2022.107513.

19. Song, Z., Li, W., Kong, H., Chen, M., Bao, Y., Wang, N., Wang, W., Liu, Z., Ma, Y., He, Y., et al. (2022). Merkel receptor-inspired integratable and biocompatible pressure sensor with linear and ultrahigh sensitive response for versatile applications. Chem. Eng. J. 444, 136481. https://doi.org/10.1016/j.cej.2022.136481.

20. Huang, Y., Fan, X., Chen, S.C., and Zhao, N. (2019). Emerging Technologies of Flexible Pressure Sensors: Materials, Modeling, Devices, and Manufacturing. Adv. Funct. Mater. 29, 1808509. https://doi.org/10.1002/adfm.201808509.

21. Pang, Y., Zhang, K., Yang, Z., Jiang, S., Ju, Z., Li, Y., Wang, X., Wang, D., Jian, M., Zhang, Y., et al. (2018). Epidermis Microstructure Inspired Graphene Pressure Sensor with Random Distributed Spinosum for High Sensitivity and Large Linearity. ACS Nano 12, 2346–2354. https://doi.org/10.1021/acsnano.7b07613.

22. Luo, Z., Chen, J., Zhu, Z., Li, L., Su, Y., Tang, W., Omisore, O.M., Wang, L., and Li, H. (2021). High-Resolution and High-Sensitivity Flexible Capacitive Pressure Sensors Enhanced by a Transferable Electrode Array and a Micropillar-PVDF Film. ACS Appl. Mater. Interfaces 13, 7635–7649. https://doi.org/10.1021/acsami.0c23042.

23. Zheng, Y., Lin, T., Zhao, N., Huang, C., Chen, W., Xue, G., Wang, Y., Teng, C., Wang, X., and Zhou, D. (2021). Highly sensitive electronic skin with a linear response based on the strategy of controlling the contact area. Nano Energy 85, 106013. https://doi.org/10.1016/j.nanoen.2021.106013.

24. Guo, X., Zhou, D., Hong, W., Wang, D., Liu, T., Wang, D., Liu, L., Yu, S., Song, Y., Bai, S., et al. (2022). Biologically Emulated Flexible Sensors With High Sensitivity and Low Hysteresis: Toward Electronic Skin to a Sense of Touch. Small 18, e2203044. https://doi.org/10.1002/smll.202203044.

25. Zhang, Y., Yang, J., Hou, X., Li, G., Wang, L., Bai, N., Cai, M., Zhao, L., Wang, Y., Zhang, J., et al. (2022). Highly stable flexible pressure sensors with a quasi-homogeneous composition and interlinked interfaces. Nat. Commun. 13, 1317. https://doi.org/10.1038/s41467-022-29093-y.

26. Lu, P., Wang, L., Zhu, P., Huang, J., Wang, Y., Bai, N., Wang, Y., Li, G., Yang, J., Xie, K., et al. (2021). Iontronic pressure sensor with high sensitivity and linear response over a wide pressure range based on soft micropillared electrodes. Sci. Bull. 66, 1091–1100. https://doi.org/10.1016/j.scib.2021.02.019.

27. Chen, Y., Qin, Y., Zhang, X., Zheng, A., and Xia, Q. (2022). Hierarchical Arete Architecture-Enabled Iontronic Pressure Sensor with High Linearity and Sensitivity.

Adv. Mater. Technol. *7*, 2200322. https://doi.org/10.1002/admt.202200322.

28. Ha, K.H., Zhang, W., Jang, H., Kang, S., Wang, L., Tan, P., Hwang, H., and Lu, N. (2021). Highly Sensitive Capacitive Pressure Sensors over a Wide Pressure Range Enabled by the Hybrid Responses of a Highly Porous Nanocomposite. Adv. Mater. *33*, e2103320. https://doi.org/10.1002/adma.202103320.

29. Cui, X., Chen, J., Wu, W., Liu, Y., Li, H., Xu, Z., and Zhu, Y. (2022). Flexible and breathable all-nanofiber iontronic pressure sensors with ultraviolet shielding and antibacterial performances for wearable electronics. Nano Energy *95*, 107022. https://doi.org/10.1016/j.nanoen.2022.107022.

30. Li, L., Zhu, G., Wang, J., Chen, J., Zhao, G., and Zhu, Y. (2023). A flexible and ultrasensitive interfacial iontronic multisensory sensor with an array of unique "cup-shaped" microcolumns for detecting pressure and temperature. Nano Energy *105*, 108012. https://doi.org/10.1016/j.nanoen.2022.108012.

31. Bai, N., Wang, L., Xue, Y., Wang, Y., Hou, X., Li, G., Zhang, Y., Cai, M., Zhao, L., Guan, F., et al. (2022). Graded Interlocks for Iontronic Pressure Sensors with High Sensitivity and High Linearity over a Broad Range. ACS Nano *16*, 4338–4347. https://doi.org/10.1021/acsnano.1c10535.

32. Bai, N., Wang, L., Wang, Q., Deng, J., Wang, Y., Lu, P., Huang, J., Li, G., Zhang, Y., Yang, J., et al. (2020). Graded intrafillable architecture-based iontronic pressure sensor with ultra-broad-range high sensitivity. Nat. Commun. *11*, 209. https://doi.org/10.1038/s41467-019-14054-9.

33. Xiao, Y., Duan, Y., Li, N., Wu, L., Meng, B., Tan, F., Lou, Y., Wang, H., Zhang, W., and Peng, Z. (2021). Multilayer Double-Sided Microstructured Flexible Iontronic Pressure Sensor with a Record-wide Linear Working Range. ACS Sens. *6*, 1785–1795. https://doi.org/10.1021/acssensors.0c02547.

34. Wu, S., Yang, C., Hu, J., Pan, M., Qiu, W., Guo, Y., Sun, K., Xu, Y., Li, P., Peng, J., and Zhang, Q. (2022). Wide-Range Linear Iontronic Pressure Sensor with Two-Scale Random Microstructured Film for Underwater Detection. ACS Omega *7*, 43923–43933. https://doi.org/10.1021/acsomega.2c05186.

35. Luo, N., Dai, W., Li, C., Zhou, Z., Lu, L., Poon, C.C.Y., Chen, S.-C., Zhang, Y., and Zhao, N. (2016). Flexible Piezoresistive Sensor Patch Enabling Ultralow Power Cuffless Blood Pressure Measurement. Adv. Funct. Mater. *26*, 1178–1187. https://doi.org/10.1002/adfm.201504560.

36. Jin, C., Xia, C., Zhang, S., Wang, L., Wang, Y., and Yan, H. (2019). A Wearable Combined Wrist Pulse Measurement System Using Airbags for Pressurization. Sensors *19*, 386. https://doi.org/10.3390/s19020386.

37. Liu, T., Gou, G.-Y., Gao, F., Yao, P., Wu, H., Guo, Y., Yin, M., Yang, J., Wen, T., Zhao, M., et al. (2023). Multichannel Flexible Pulse Perception Array for Intelligent Disease Diagnosis System. ACS Nano *17*, 5673–5685. https://doi.org/10.1021/acsnano.2c11897.

38. Song, Z., Li, W., Bao, Y., Wang, W., Liu, Z., Han, F., Han, D., and Niu, L. (2018). Bioinspired Microstructured Pressure Sensor Based on a Janus Graphene Film for Monitoring Vital Signs and Cardiovascular Assessment. Adv. Electron. Mater. *4*, 1800252–1800260. https://doi.org/10.1002/aelm.201800252.

39. Ouyang, H., Tian, J., Sun, G., Zou, Y., Liu, Z., Li, H., Zhao, L., Shi, B., Fan, Y., Fan, Y., et al. (2017). Self-Powered Pulse Sensor for Antidiastole of Cardiovascular Disease. Adv. Mater. *29*, 1703456. https://doi.org/10.1002/adma.201703456.

40. An, Q., Gan, S., Xu, J., Bao, Y., Wu, T., Kong, H., Zhong, L., Ma, Y., Song, Z., and Niu, L. (2019). A multichannel electrochemical all-solid-state wearable potentiometric sensor for real-time sweat ion monitoring. Electrochem. Commun. *107*, 106553. https://doi.org/10.1016/j.elecom.2019.106553.

41. Kong, H., Song, Z., Xu, J., Qu, D., Bao, Y., Wang, W., Wang, Z., Zhang, Y., Ma, Y., Han, D., and Niu, L. (2020). Untraditional Deformation-Driven Pressure Sensor with High Sensitivity and Ultra-Large Sensing Range up to MPa Enables Versatile Applications. Adv. Mater. Technol. *5*, 2000677. https://doi.org/10.1002/admt.202000677.

42. Song, Z., Li, W., Kong, H., Bao, Y., Wang, N., Wang, W., Ma, Y., He, Y., Gan, S., and Niu, L. (2022). Enhanced energy harvesting performance of triboelectric nanogenerator via efficient dielectric modulation dominated by interfacial interaction. Nano Energy *92*, 106759. https://doi.org/10.1016/j.nanoen.2021.106759.

43. Li, W., Song, Z., Zhong, J., Qian, J., Tan, Z., Wu, X., Chu, H., Nie, W., and Ran, X. (2019). Multilayer-structured transparent MXene/PVDF film with excellent dielectric and energy storage performance. J. Mater. Chem. C *7*, 10371–10378. https://doi.org/10.1039/c9tc02715g.

STAR★METHODS

KEY RESOURCES TABLE

REAGENT or RESOURCE	SOURCE	IDENTIFIER
Chemicals, peptides, and recombinant proteins		
Ti_3AlC_2	Jilin 11 Technology Co., Ltd (Jilin, China)	CAS 196506-01-1
PVDF Solef 1010	Solvay (Shanghai, China)	CAS 24937-79-9
Lithium fluoride	Sigma-Aldrich	CAS 7789-24-4
Hydrochloric acid	Sigma-Aldrich	CAS 2647-01-0
N, N dimethylformamide	Beijing Chemical Works (Beijing, China)	CAS 68-12-2
PDMS SYLGARD 184	Dow Corning (Shanghai, China)	CAS 9016-00-6
Software and algorithms		
Origin Pro 8	Originlab	https://www.originlab.com/
COMSOL Multiphysics 5.4	COMSOL	https://cn.comsol.com/

RESOURCE AVAILABILITY

Lead contact

Further information and requests for resources and reagents should be directed to and will be fulfilled by the Lead Contact, Zhongqian Song (szq0819@163.com).

Materials availability

This study did not generate new unique reagents.

Data and code availability

- All data reported in this paper will be shared by the lead contact upon request.

- This paper does not report original code.

- Any additional information required to reanalyze the data reported in this paper is available from the lead contact upon reasonable request.

METHOD DETAILS

Materials and instruments

Ti_3AlC_2 MAX phase (400 mesh) was purchased from Jilin 11 Technology Co.Ltd (Changchun, China). PVDF (Solef 1010) was provided by Solvay S.A. Lithium fluoride (LiF) and hydrochloric acid (HCl) were purchased from Sigma Aldrich and used as received. N, N-dimethylformamide (DMF) used in this work was obtained from Beijing Chemical Works (Beijing, China). Graphene solution was prepared via our reported method.[40,41] $Ti_3C_2T_x$ MXene solution was synthesized by selective etching of Al from Ti_3AlC_2 MAX phases and delaminated using minimally intensive layer delamination method.[42,43] The pulse waveforms were recorded by an LCR Meter (Keysight E4980A) and the second derivatives were transformed using Origin 8.5 Software. The scanning electrical microscopy was carried out using a Phenom ProX at an acceleration of 10 kV. The surface roughness was measured via a 3D Optical Profilometer (ST400, NANOVEA, USA). A computer-controlled movable stage (Lianyi XYZM100H-50, Shanghai) was used to apply the pressure. A force gauge (Shandu SH-500B) was used for precise real-time pressure acquisition. The pressure and capacitance signals are simultaneously recorded via a homemade program.

Preparation of the even-surfaced conductive electrode

The patterned mask engraved by laser engraver is attached on the polyfluortetraethylene (PTFE) plate which is preheated on a heater (70°C). The graphene nanoflakes were dispersed in ethanol by sonication for 10 min to obtain a homogenous suspension with a concentration of 2 mg mL^{-1}. The graphene suspension was diluted by ethanol (1:3, v/v) and then sprayed onto cleaned PTFE plate at 70°C by an airbrush with

0.2 mm nozzle size and 50 psi operating pressure. The liquid PDMS precursor and a curing agent (Dow Corning Sylgard 184, the weight ratio of base to cross linker was 10:1) are poured onto the PTFE plate, scraped with a glass rod with a transparent rubber ring (∼1 mm height) to evenly cover the graphene electrode, and then cured at 80°C for 30 min. The even-surfaced conductive electrode is peeled off from the PTFE plate and cut into desirable sizes for further use.

Preparation of microstructured ionic polymer film

MXene dispersion (1 mL, 5 mg /mL) and graphene powder (10 mg) were mixed and diluted to 10 mL with distilled water with the aid of sonication. The patterned MXene/graphene conductive electrode was obtained via filtering the above mixed dispersion using a patterned filter membrane (0.45 μm) as a mask. The electrode was transferred onto glass substrate and rolled via a glass rod before removal of the filter membrane. PVDF (3 g) powder and DMF (22 g) are mixed and stirred for 8 h at room temperature. The above solution (5.38 g) was mixed with PS microspheres (0 g, 0.08 g, 0.16 g, 0.24 g) and ionic liquids (0 g, 0.0717 g, 0.1614 g, 0.2767 g, 0.4304 g) and then are stirred to obtain the mixed solution with a certain concentration of ionic liquids. The as-prepared mixed dispersion was directly cast onto the glass substrate with the MXene/graphene electrode, and then dried at 70°C for 15 min to obtain the ionic polymer film. The film is peeled off from the glass and cut into suitable size for further use.

Fabrication and application of the iontronic pressure sensor

The iontronic pressure sensor was fabricated by assembling the even-surfaced conductive electrode on the microstructured ionic polymer film and then encapsulated by polyimide (PI, 30 μm) tape. Two silver coated copper wires were connected with the two electrodes for electrical connection with silver paste. An asymptomatic male volunteer (25 years old) was recruited for versatile applications, such as human motion and pulse waveforms monitoring. The iontronic pressure sensor was placed right above the radial artery at different locations and fixed with medical tape to collect the arterial pulse waveforms. According to the guidelines of the Institutional Research Ethics Board, all subjects gave their informed consent before the experiments. A groove (width 15 mm, length 20 mm, depth 3 mm) under the insole was pre-designed to avoid the local stress concentration and then the pressure sensor was put into the groove for human motion monitoring.

Finite element analysis

Finite element analysis was adopted to predict the shape deformation and stress distribution induced by the pressure. Finite element analysis was carried out by the COMSOL Multiphysics software. The Young's modulus and Poisson's ratio of high-modulus materials are 1 GPa and 0.39. The Young's modulus and Poisson's ratio of low-modulus materials are 1 MPa and 0.49.